ACS Catalysis

Research Article

pubs.acs.org/acscatalysis

Tuning Nb−Pt Interactions To Facilitate Fuel Cell Electrocatalysis

Shraboni Ghoshal,[†] Qingying Jia,[†] Michael K. Bates,[†,#] Jingkun Li,[†] Chunchuan Xu,[‡] Kerrie Gath,[‡] Jun Yang,[‡] James Waldecker,[‡] Haiying Che,[§] Wentao Liang,[∥] Guangnan Meng,[⊥] Zi-Feng Ma,[§] and Sanjeev Mukerjee*[,†]

[†]Northeastern University for Renewable Energy Technology, Department of Chemistry & Chemical Biology, Northeastern University, Boston, Massachusetts 02115, United States

[‡]Ford Motor Company, Dearborn, Michigan 48121, United States

[§]Shanghai Electrochemical Energy Devices Research Center, Department of Chemical Engineering, Shanghai Jiao Tong University, Shanghai 200240, People's Republic of China

[∥]Department of Biology, Northeastern University, Boston, Massachusetts 02115, United States

[⊥]ULVAC Technologies, Inc., 401 Griffin Brook Drive, Methuen, Massachusetts 01844, United States

Supporting Information

ABSTRACT: High stability, availability of multiple oxidation states, and accessibility within a wide electrochemical window are the prime features of Nb that make it a favorable candidate for electrocatalysis, especially when it is combined with Pt. However, Nb has been used as a support in the form of oxides in all previously reported Pt−Nb electrocatalysts, and no Pt−Nb alloying phase has been demonstrated hitherto. Herein, we report a multifunctional Pt−Nb composite ($PtNb/NbO_x$-C) where Nb exists both as an alloying component with Pt and as an oxide support and is synthesized by means of a simple wet chemical method. In this work, the Pt−Nb alloy phase has been firmly verified with the help of multiple spectroscopic methods. This allows for the experimental evidence of the theoretical prediction that Pt−Nb alloy interactions improve the oxygen reduction reaction (ORR) activity of Pt. In addition, such a combination of multiphase Nb brings up myriad features encompassing increased ORR durability, immunity to phosphate anion poisoning, enhanced hydrogen oxidation reaction (HOR) activity, and oxidative carbon monoxide (CO) stripping, making this electrocatalyst useful in multiple fuel cell systems.

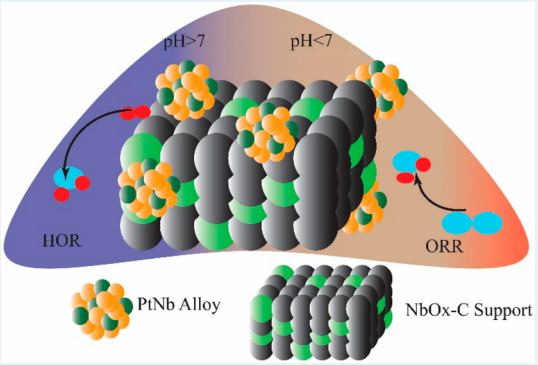

KEYWORDS: *Pt−Nb alloy, electronic effect, oxygen reduction reaction, hydrogen oxidation reaction, in situ X-ray absorption spectroscopy*

INTRODUCTION

Evolution of electrocatalytic energy conversion processes is crucial to mitigate global warming and curtail our need for fossil energy. This demands the smart design of electrocatalysts that are economical, durable, and highly efficient. More than two decades of research[1,2] on modification of Pt surfaces (alloying, ad-metal, nanoparticle, core−shell, etc.) have provided significant improvements in activity (ORR and HOR) and durability while lowering the Pt loading. The choice of binary metal is dictated by several factors, principal among which is the extent of solid solution formation (i.e., substitutional effect) and its concomitant effect on the electronic states of Pt. Extensive studies on Pt alloys with first-row transition elements[1,3] are available where enhanced ORR activity is exhibited by the catalyst. Such superior ORR activity has been explained as a function of lattice strain[4] and ligand effect,[5−7] though depending on the transition metal and its specific segregation potential[8,9] various degrees of Pt skin effects have been determined, resulting in various core−shell structures.[10,11] It should be noted that in most of these previous works Pt was alloyed with first-row transition elements with smaller atomic sizes. As shown by several prior reports, the resulting alloy therefore exhibits lattice contraction (strain effect) and a possible charge transfer between Pt and the alloying element (ligand effect).[12,13] At the anode, composites of Pt with surface specific oxophilic moieties such as Ru, Mo, etc. have been invoked in the case of anodic reformate tolerance as well as direct oxidation of liquid fuels such as methanol etc.[14,15]

In this report we probe both the ORR (acidic pH) and HOR (alkaline pH), both kinetically challenged in their own aqueous domains with the choice of Nb as an alloying element. Nb, being larger in atomic size in comparison to Pt, has the potential of causing lattice strain in the opposite direction in comparison to the wealth of prior Pt alloys where lattice

Received: March 31, 2017
Revised: May 30, 2017
Published: June 15, 2017

© XXXX American Chemical Society

DOI: 10.1021/acscatal.7b01061
ACS Catal. 2017, 7, 4936−4946

Scheme 1. Synthesis of PtNb/NbO$_x$-C Catalyst

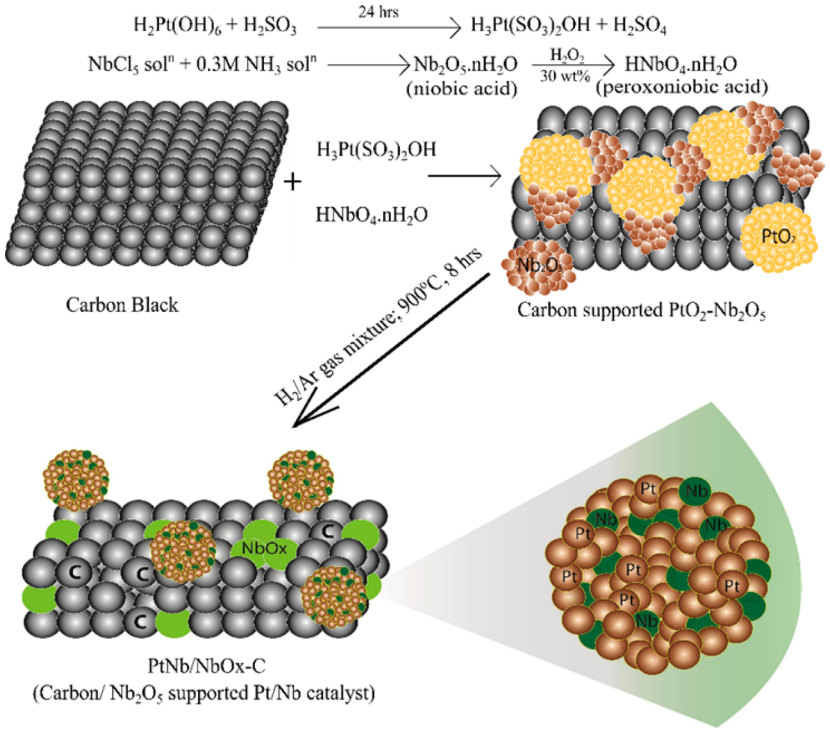

contraction occurs.[16,17] With properties such as high oxophilicity,[18] exceptional stability in acid,[19,20] wide electrochemical window, and availability of multiple oxidation states,[21] Nb constitutes an interesting candidate. A vast literature on Pt−Nb bimetallic systems exists, mostly based on niobium oxide as stable supports for Pt (Adzic et al.[22,23] and Mitlin et al.[24]). Relatively few reports have specifically examined the correlation of Nb used as an alloying element and its role in changing the inherent electrocatalytic behavior of Pt. Due to its strong oxophilicity and high negative reduction potential, there is a thermodynamic barrier which restricts the formation of zerovalent Nb under regular (<1000 °C) heat treatment temperatures, and hence the formation of alloys between Pt and Nb is scarce in the literature.[25]

During the ORR in alkaline systems, there are nominal overpotential losses due to the occurrence of an outer sphere electron transfer that enables the use of several non-platinum catalysts as cathodes.[26−28] Meanwhile in acid electrolyte, high performance losses and requirement of platinum catalysts for the ORR brings out challenges pertaining to the cost effectiveness of the system. Niobium oxide, when present as a support in platinum catalysts, has been reported to enhance the ORR catalytic performance in acidic pH despite having no intrinsic catalytic activity of its own.[29] For example, the hydrophilic Nb_xO_y materials are known to offer better platinum mass utilization toward the ORR.[24] In addition to this, the existence of a synergistic cocatalytic effect between platinum and niobium oxide support prevents aggregation of platinum particles during fuel cell operation.[30] In the case of PtNb alloys, Nørskov et al.[31] have theoretically predicted the adsorption strength of oxygen species on PtNb alloy to be in the favorable range, predicting superior intrinsic activity toward the ORR in comparison to Pt/C. Nonetheless, this has not been verified experimentally due to the lack of proper platinum−niobium alloys hitherto.

In alkaline electrolyte HOR kinetics is a major challenge,[32,33] resulting in an overvoltage of several hundred millivolts at moderate current densities. Here Pt is not a nonpolarizable electrode in contrast to the case at acidic pH.[34,35] The observed sluggish HOR kinetics in alkaline electrolyte in comparison to that for acid electrolyte is explained by two different theories: namely, (a) binding energy theory[36−38] and (b) reactive OH_{ad} species theory.[39] Theory (a) states that an increase in M−H_{ad} bond strength at higher pH decelerates the HOR rate.[40] This theory takes into account that the Volmer reaction (M−H_{ad} + $OH^- \rightarrow M + H_2O + e^-$) is most likely the rate-determining step of the HOR,[41] thereby putting the onus on M−H_{ad} binding strength being the sole descriptor of the HOR rate. However, the availability of OH^- can potentially influence the rate of the Volmer step, as is evident from the reaction, which gave rise to the second school of thought. The HOR on a Pt surface occurs at potentials lower than the potential of zero charge (PZC) where the surface is negatively charged. Theory (b) states that the nonavailability of reactive OH_{ad} species (due to electrostatic repulsion) at the electrical double layer causes slow alkaline HOR kinetics.[39] As a matter of fact, faster HOR kinetics in alkaline electrolyte is seen when Pt is alloyed with "oxophilic" metals such as Ru and Ni that are believed to act as the source for furnishing reactive OH_{ad} species at the electrode interface.[39] No prior HOR study on Pt−Nb system exists, but the aforementioned interesting properties of a Pt−Nb alloy−NbO_x composite such as oxophilicity and alloy interaction between Pt and Nb are expected to have conducive effects on the alkaline HOR catalysis.

In this report, we present a carbon-supported platinum−niobium alloy catalyst (PtNb/NbO$_x$-C) synthesized by an innovative route. We have strategically designed the composite to manipulate the base metal Nb in two ways: (a) as Nb oxide to circumvent catalyst degradation and (b) as an alloying metal for tweaking the electronic and geometric properties of

DOI: 10.1021/acscatal.7b01061
ACS Catal. 2017, 7, 4936−4946

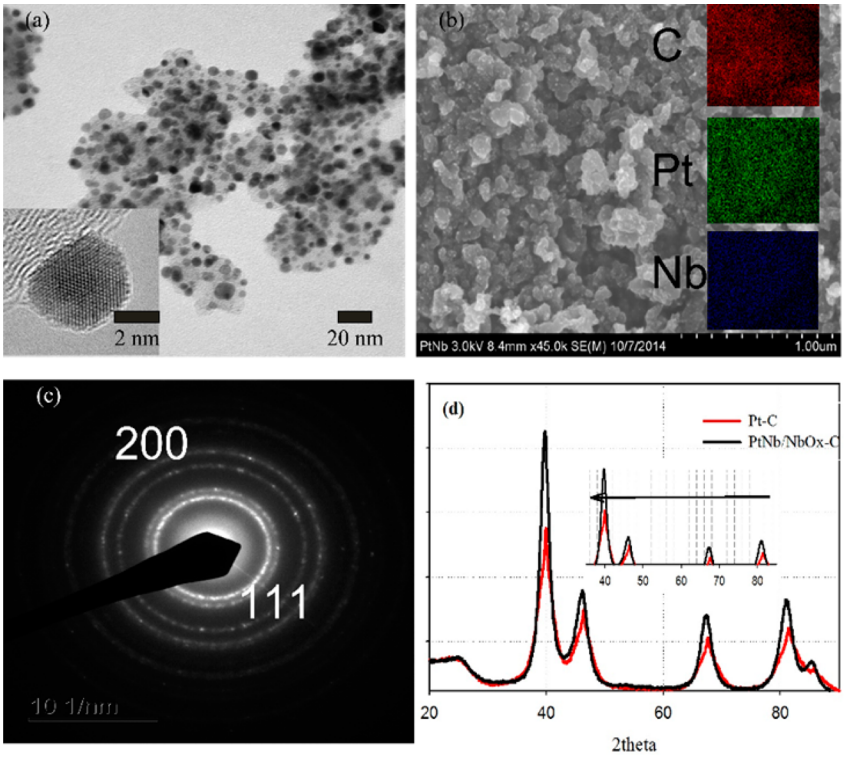

Figure 1. (a) High-resolution and low-resolution TEM of PtNb/NbO_x-C catalyst. (b) SEM and elemental mapping results obtained using SEM-EDX. (c) SAED image of PtNb/NbO_x-C. (d) X-ray diffraction patterns of Pt/C (standard) and PtNb/NbO_x-C catalyst.

platinum. With the help of an X-ray diffraction (XRD) study, X-ray photoelectron spectroscopy (XPS), and in situ X-ray absorption spectroscopic (XAS) experiments, we have validated the structure of the catalyst in detail. In addition to ORR experiments where PtNb/NbO_x-C catalyst exhibited superior performance in comparison to Pt/C, we have performed CO adsorption experiments to provide insight into the role of Nb atoms in terms of electronic and bifunctional effects. Our PtNb/NbO_x-C catalyst has been compared to controls, i.e., Pt/NbO_x-C (where Nb is present in form of oxide support) as well as pure Pt/C, to delineate the contributions of binding energy and reactive OH_{ad} effects toward alkaline HOR. To the authors' knowledge, this is the first time a Pt−Nb alloy interaction has been established by structure-sensitive experiments in a Pt−Nb electrocatalyst system having multifaceted catalytic properties.

RESULTS AND DISCUSSION

Catalyst Synthesis. Scheme 1 illustrates the synthesis of the PtNb/NbO_x-C catalyst. One of the most critical factors that determines the state of Nb atoms (as an alloy component or as an oxide support) is the sequence of deposition of Pt and Nb (in form of oxides) from their respective precursor solutions. Codeposition of the metal oxides (Pt and Nb) is crucial to maintain an even distribution among Pt and Nb atoms, which results in a better alloy formation. $H_3Pt(SO_3)_2OH$ is a chemically stable solution and is commonly used as a precursor to obtain PtO_2 electrochemically or chemically under oxidizing conditions.[42] In this modified method, the use of $H_3Pt(SO_3)_2OH$ and H_2O_2 ensures the formation of monodispersed, small particles.[43] The peroxoniobic acid, along with a calculated excess of hydrogen peroxide, is used to decompose $H_3Pt(SO_3)_2OH$ into PtO_2 while Nb is precipitated as $Nb_2O_5{\cdot}nH_2O$. The final heat treatment at high temperature under reductive atmosphere is an essential step, as it promotes the reduction of PtO_2 to Pt and of Nb_2O_5 to zero valent Nb (enabling alloy formation with Pt) and Nb oxides, where Nb attains multiple oxidation states.

Physicochemical Characterizations. Figure 1a shows the transmission electron microscopy (TEM) image of the synthesized PtNb/NbO_x-C catalyst as dispersed on a Cu grid under low- and high-resolution (inset) modes. The catalyst particles are found to be homogeneously dispersed with an average particle size of 4−5 nm. The well-defined lattice fringes (Figure 1a, inset) confirm the high crystallinity of the supported metal clusters. The scanning electron microscopy (SEM) and electron dispersive X-ray spectroscopy (EDX) images in Figure 1b give a general morphological idea of the catalyst. The SEM-EDX elemental mapping images of C, Pt, and Nb are juxtaposed in Figure 1b. They show that Nb and Pt are evenly distributed on the carbon support.

The selected area electron diffraction (SAED) pattern in Figure 1c shows concentric rings consisting of discrete diffraction spots, indicating the high crystallinity of the material in agreement with the TEM results. The lattice spacings of 2.29 and 1.98 Å can be indexed to te {111} and {200} planes of the Pt cubic lattice, respectively. The representative XRD of PtNb/NbO_x-C and Pt/C (as standard) collected from 2θ values of 20−90° are shown in Figure 1d. On the basis of Pt {111} crystallite line broadening, the Pt crystallite size in PtNb/NbO_x-C was found to be 3.3 nm. PtNb/NbO_x-C exhibits a pattern corresponding to the Pt cubic phase with the peaks shifted toward lower 2θ values. The lattice constant for PtNb/NbO_x-C was found to be 3.942, whereas for Pt/C, the lattice constant value was 3.912. Considering the larger atomic radius of Nb (145 pm) in comparison to that of Pt (135 pm), such a shift in 2θ value is expected per Vegard's law.[44,45] This

DOI: 10.1021/acscatal.7b01061
ACS Catal. 2017, 7, 4936−4946

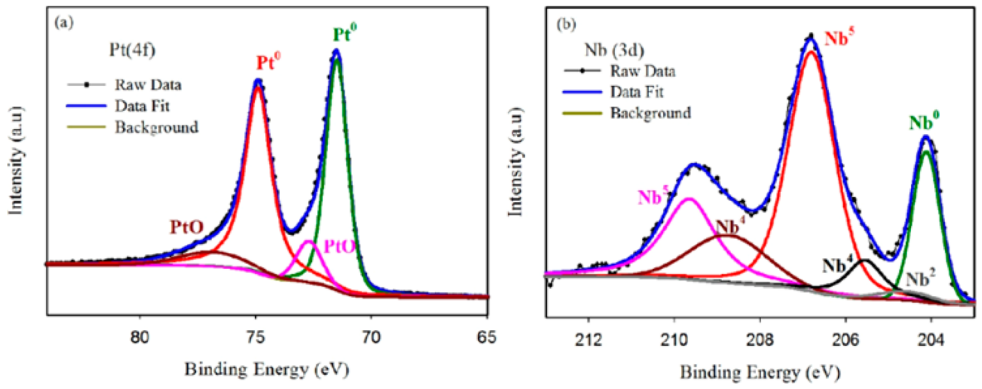

Figure 2. XPS high-resolution spectra of PtNb/NbO_x-C catalyst for (a) Pt 4f and (b) Nb 3d binding energy regions.

observation in addition to the changed lattice constant values strongly suggests the formation of a Pt−Nb "alloy" phase which has not been reported experimentally so far. Since catalysis is a surface phenomenon, it is crucial to evaluate the surface species present in the PtNb/NbO_x-C catalyst; this has been conducted using high-resolution XPS spectra collected at the relevant Pt and Nb binding energy regions (Figure 2). Pt 4f spectra strongly suggest that Pt mostly exists as a metal on the surface, along with some traces of PtO. Nb 3d spectra bring out the multiple oxidation states of Nb present on the surface. While Nb(V) oxide and metallic Nb(0) are the most dominant species detected, traces of Nb(IV) and Nb(II) oxides can also be identified at the surface. Hence, XPS results confirm the presence of multiple oxidation states of Nb, including metallic Nb on the surface. Quantification results from XPS reveal that the catalyst contains 64% C, 20.4% Pt, 5% Nb, and 10.6% O. Further confirmation of the composition was done using inductively coupled plasma mass spectroscopy (ICP-MS) and the results were similar to that obtained by XPS. XPS spectra of a niobia-supported Pt catalyst were found to be devoid of any Nb(0) peak (Figure S1 in the Supporting Information). XAS experiments (vide infra) further ascertain the formation of Pt−Nb alloy and give vital information on the electrochemical properties of the PtNb/NbO_x-C catalyst.

X-ray Absorption Spectroscopy. In situ XAS measurements were conducted at both Pt L_3 and Nb K edges as a function of applied potentials to quantitatively determine the local structure of the PtNb/NbO_x-C catalyst. The Nb data remain unchanged within a wide potential range from 0.1 to 1.5 V in both N- and O_2-saturated electrolyte (Figure S2 in the Supporting Information), which indicates that Nb does not undergo a redox transition within the entire fuel cell operating potential range. In situ X-ray absorption near edge structure (XANES) at the Nb K-edge (Figure 3a) reveals that the bulk-average oxidation state of the Nb in PtNb/NbO_x-C is close to +2, as illustrated by overlapping XANES spectra of a NbO standard. However, the Fourier transform of the extended X-ray absorption fine structure (EXAFS) of the catalyst is drastically different from that of the NbO standard (Figure 3b). PtNb/NbO_x-C exhibits a prominent peak in the Nb−Nb/Pt scattering region (~2.5 Å, without phase correction), but the Nb−O peak around 1.5 Å (without phase correction) has a relatively low intensity. This suggests that the Nb in the catalysts can be divided into two categories: one alloyed with Pt and one present in the form of Nb oxides. The coexistence of the multiple phases of Nb makes the FT-EXAFS fitting of the Nb data infeasible. On the other hand, the FT-EXAFS fitting of

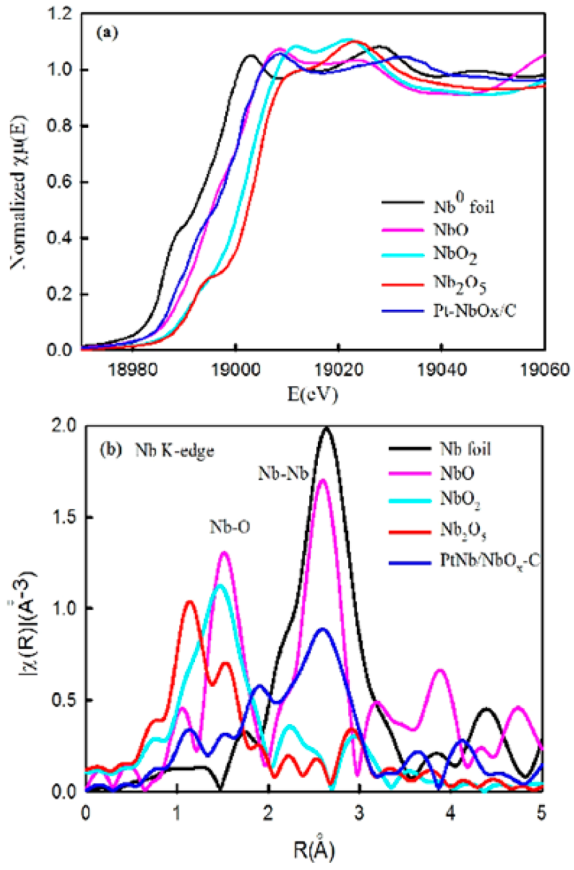

Figure 3. (a) In situ XANES and (b) FT-EXAFS data of the PtNb/NbO_x-C catalyst. The data were collected at the Nb K edge at 0.54 V vs RHE in N_2-saturated 0.1 M $HClO_4$ electrolyte in a flow cell. The XAS data of several standard Nb oxides collected at the same beamline are also included as references.

the Pt edge data can be well fitted, which provides direct evidence of the Pt−Nb interaction, as shown in Figure 4.

The abundance of Pt−Nb bonds in the catalyst has been quantitatively evaluated by EXAFS analysis (Table 1) at the Pt L_3 edge. By inclusion of a Pt−Nb scattering path into the fitting model, a reasonably good fit was achieved, providing the coordination number of Pt−Nb (N_{Pt-Nb}) as 2.3, which is significant in comparison to the fitting uncertainty (0.3) (Table 1), In addition, the measured Pt−Pt and Pt−Nb bond distances in PtNb/NbO_x-C were longer than that of Pt/C (Table 1), in agreement with the larger lattice constant given by XRD

DOI: 10.1021/acscatal.7b01061
ACS Catal. 2017, 7, 4936−4946

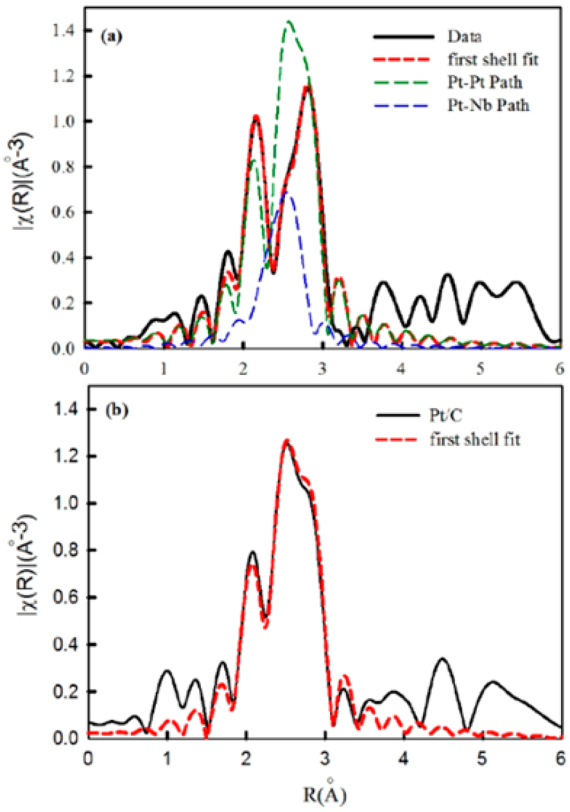

Figure 4. In situ FT-EXAFS data and the corresponding fitting results of the (a) PtNb/NbO_x-C and (b) Pt/C catalysts. The data were collected at the Pt L_3 edge at 0.54 V vs RHE in N_2-saturated 0.1 M $HClO_4$ electrolyte. The fitting parameters are given in Table 1.

(Figure 1d). These results further provide conclusive evidence for the alloying of Pt−Nb in the PtNb/NbO_x-C catalyst. To the best of the authors' knowledge, this is the first time the Pt−Nb alloying phase has been unambiguously demonstrated. Since the Nb atoms present in the alloying phase are present in 0 oxidation state, the bulk average oxidation state of +2 (estimated from XANES at the Nb K-edge) points to the coexistence of Nb^0 and NbO_x, where $x \geq 1$. This has already been demonstrated in the XPS data, where multiple oxidation states of Nb were identified.

In situ XAS measurements show that the Pt white line intensities for both PtNb/NbO_x-C and Pt/C increase with increasing potentials (Figure 5). This trend is caused by the charge transfer from Pt surface to the oxygenated adsorbates and thus reflects the progressive accumulation of the oxygenated adsorbates onto the Pt surface with increasing potentials. Assuming the Pt surface is free of adsorbates at 0.54 V (the double-layer region), the relative oxygen coverage at the potential V can be represented by the subtractive $\Delta\mu(V) = \mu(V) - \mu(0.54\ V)$.[46] This subtractive technique, referred to as the $\Delta\mu$ method, involved subtraction of XANES spectra measured under controlled conditions such as 0.54 V (Ar purged). where minimum surface adsorbates are expected. minus spectra where surface adsorbed species were expected. The comparison of the $\Delta\mu(V)$ values between PtNb/NbO_x-C and Pt/C as displayed in Figure 5c clearly shows the late onset of adsorption of oxygenated species via water activation on PtNb/NbO_x relative to Pt/C; this is closely related to an enhanced ORR activity, as illustrated in the next section. The suppression of the formation of surface-adsorbed oxygenated species cannot be ascribed to the compressive-strain effect, as the Pt−Pt bond distance in PtNb/NbO_x-C is larger in comparison to Pt/C, and the resultant tensile strain presumably facilitates oxygen adsorption by strengthening the Pt−O binding energy.[47,48] It should be noted that Nørskov et al.[31] have predicted that the Pt−O binding energy of the PtNb alloy is weaker than that of pure Pt, which therefore has to be attributed to the ligand effect induced by Nb. It is important to emphasize that there is a key difference between the Pt−Nb system and the widely studied Pt alloys with first-row transition series such as the Pt−(Co/Ni) catalytic system. Surface Co and Ni undergo rapid dissolution in acid and are selectively leached out from the catalyst particles in acid media. As a result, the alloys eventually form a core−shell structure with pure Pt overlayers, wherein the ligand effect disappears or is severely attenuated.[49,50] In contrast, Nb is insoluble in acid, which ensures that the ligand effect induced by Nb stays germane during the entire period of operation. Our results provide the first experimental proof for the superior ORR activity of Pt as a result of the ligand effect of Nb, a fact which was predicted theoretically.[31] It should be noted that such suppressed adsorption of oxygenated species was also observed on the Pt/NbO_x/C system, wherein the Pt was supported onto Nb, which was ascribed to active site−support synergy and the ability of Nb to getter oxygen in preference to adjacent Pt.[5,22]

Oxygen Reduction Reaction in Acid on PtNb/NbO_x-C Catalyst. We benchmarked the electrocatalytic properties of the PtNb/NbO_x-C catalyst using a commercial Pt/C catalyst (40% by weight, 3 nm Pt particles supported on Vulcan XC-72R). Pt/C exhibits a typical cyclic voltammogram (CV) with distinct H_{UPD} adsorption/desorption peaks (Pt + $H_3O^+ \leftrightarrow$ Pt−H_{ad} + H_2O) between 0.05 and 0.35 V (Figure 6a, inset). The same features are also present in the CV of PtNb/NbO_x-C, though slightly diminished. The electrochemical surface areas (ECSAs) derived from the H_{UPD} were found to be 45 m^2/g_{Pt} for PtNb/NbO_x-C, in comparison to 65 m^2/g_{Pt} for Pt/C. The lower ECSA of the PtNb/NbO_x-C catalyst is most likely due to presence of catalyst agglomerates caused by the heat treatment during the synthesis in addition to the presence of niobium

Table 1. Summary of EXAFS Fitting Results of the Data of the PtNb/NbO_x-C and Pt/C Catalysts Collected at the Pt L_3 Edge at 0.54 V vs RHE in N_2-Saturated 0.1 M $HClO_4$ Electrolyte[a]

	Pt−Pt scattering			Pt−Nb scattering			
catalyst	R (Å)	N	σ^2 (10^{-3} Å^2)	R (Å)	N	σ^2 (10^{-3} Å^2)	E_0 (eV)
PtNb/NbO_x-C	2.771(2)	8.1(7)	4.6(5)	2.792(7)	2.3(3)	4.6(5)	7.2(5)
Pt/C	2.753(3)	8.4(9)	5.0(5)				7.5(9)

[a] S_0^2 is fixed at 0.84 for Pt, as obtained by fitting the reference foil. Fits were done in R space, with $k^{1,2,3}$ weighting. For Pt, 1.23 < R < 3.09 Å and Δk = 3.1−13.4 Å^{-1} were used; for PtNb/NbO_x-C, 1.3 < R < 3.06 Å and Δk = 2.539−11.646 Å^{-1} were used. Values in parentheses indicate the largest statistical error of all of the least-squares fits determined by ARTEMIS.

DOI: 10.1021/acscatal.7b01061
ACS Catal. 2017, 7, 4936−4946

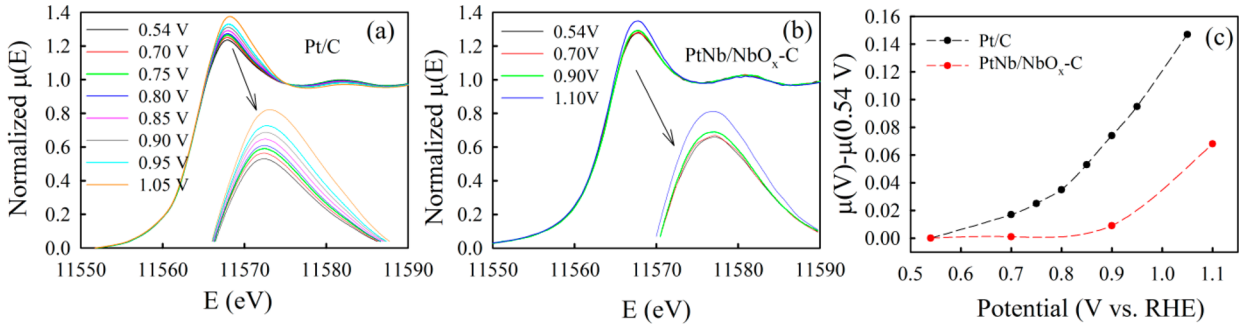

Figure 5. In situ XANES data of the (a) Pt/C and (b) PtNb/NbO$_x$-C catalysts collected at the Pt L_3 edge at various potentials in N_2-saturated 0.1 M $HClO_4$ electrolyte. (c) Changes in absorption peaks $\mu(V) - \mu(0.54\ V)$ derived from (a) and (b), as a function of applied potentials.

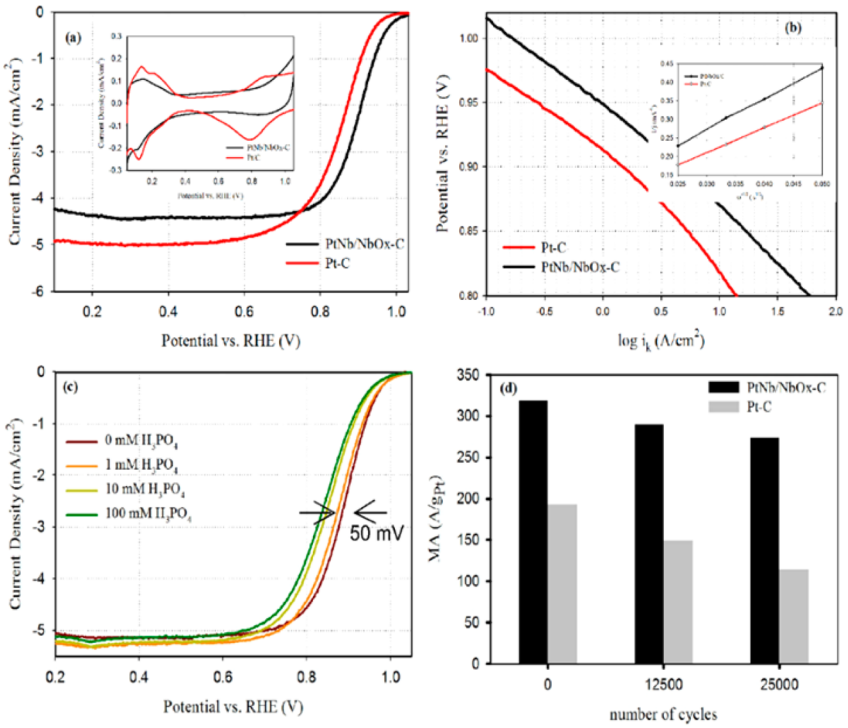

Figure 6. (a) ORR polarization curves for Pt/C and PtNb/NbO$_x$-C recorded at room temperature in O_2-saturated 0.1 M $HClO_4$ at 1600 rpm at 20 mV sec^{-1} and (inset) CV of Pt/C and PtNb/NbOx-C in Ar-saturated 0.1 M $HClO_4$ solution collected at a sweep of 20 mV s^{-1}. (b) Mass transport corrected Tafel plots of Pt/C and PtNb/NbO$_x$-C catalyst using the results in (a) and (inset) K-L plots of Pt/C and PtNb/NbO$_x$-C. (c) ORR polarization curves of PtNb/NbO$_x$-C collected at room temperature in O_2-saturated 0.1 M $HClO_4$ with various amounts of H_3PO_4 doped into the electrolyte. (d) Comparison of mass activity between Pt/C and PtNb/NbO$_x$-C with cycling in Ar-saturated 0.1 M $HClO_4$ solution.

species on the surface. The formation of Pt−OH_{ad} starts at ∼0.6 V in Pt/C catalyst because of water activation ($2H_2O$ + Pt(M) → Pt(M)OH_{ad} + H_3O^+ + e^-). As shown earlier,[51] this reaction impedes the ORR by blocking ORR active sites and is one of the major reasons of ORR activity loss in Pt-based catalysts. This process, however, is delayed in the case of PtNb/NbO$_x$-C, as suggested by the anodic shift of the redox peak in the CV (Figure 6a, inset) indicating suppressed oxygen coverage (see $\Delta\mu(V)$ as shown in Figure 5c). As expected from the diminished site-blocking effect, PtNb/NbO$_x$-C exhibits superior ORR activity in comparison to Pt/C, as shown in Figure 6a. Mass transport corrected Tafel plots for PtNb/NbO$_x$-C and Pt/C (Figure 6b) indicate no change in ORR mechanism in the two catalysts. The total number of electrons transferred during the ORR was determined from the K-L plots (Figure 6b, inset) and was found to be ∼4 for both Pt/C and PtNb/NbO$_x$-C. The higher ORR activity of PtNb/NbO$_x$-C, despite having a lower ECSA, can be attributed to the higher specific activity enabled by the ligand effect originating from the Pt−Nb alloy formation (as predicted by Nørskov[31] on the basis of a computational screening in 2009).

As mentioned earlier, Nb is known to have exceptional stability in acids and its oxides tend to influence the electronic features of Pt metal via strong metal−metal oxide interactions. An interplay of various effects, such as electrostatic phenomena (work function shift), band structure effects (d band center shift), and conductivity (density of states at the Fermi level), is expected to affect the activity of Pt in the presence of Nb oxides.[52] These facts largely work toward increasing the electrochemical stability of the noble-metal catalyst and making it more durable and tolerant toward anion poisoning and catalyst degradation. To test this hypothesis, PtNb/NbO$_x$-C was subjected to anion poisoning by introducing calculated amounts of phosphoric acid as dopants to O_2 saturated 0.1 M

DOI: 10.1021/acscatal.7b01061
ACS Catal. 2017, 7, 4936−4946

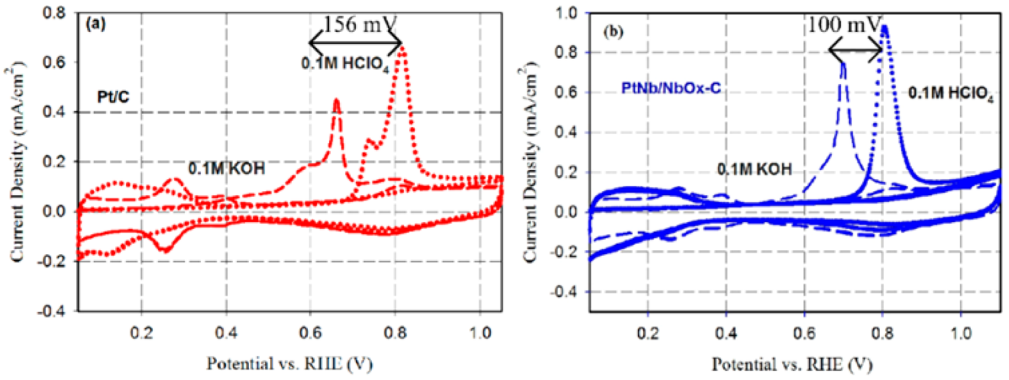

Figure 7. CO stripping data for (a) Pt/C and (b) PtNb/NbO_x-C in 0.1 M $HClO_4$ (dotted) and 0.1 M KOH (dashed) collected at 10 mV s^{-1} sweep rate. Loading of Pt 20 $\mu g/cm^2$.

$HClO_4$ solution (Figure 6c). With an increasing dopant concentration, the half-wave potential shifts cathodically, resulting in a 50 mV shift from 0 mM H_3PO_4 to 100 mM H_3PO_4, whereas a net cathodic shift of 110 mV was observed for Pt/C under the same experimental conditions (Figure S3 in the Supporting Information). Hence, modifying the Pt structure with Nb mitigates phosphate anion poisoning to a substantial extent. This trend can be envisioned in terms of the surface niobium species that impart electrostatic repulsion to phosphate anions and alleviate the poisoning of Pt active sites by the anions. Furthermore, the presence of surface Nb species significantly dilutes the fcc sites of Pt (one surface Nb atom can at most destroy four Pt fcc sites) and in turn inhibits attachment of PO_4^{3-} that selectively binds to the Pt fcc sites. A somewhat similar effect has been reported by us earlier using a PtNi alloy.[53]

Figure 6d compares the results of durability measurements obtained from RDE experiments in O_2-saturated 0.1 M $HClO_4$ for Pt/C and PtNb/NbO_x-C. For the testing, the catalysts were subjected to a square-wave process between 0.1 and 1.0 V, with each potential held for 3 s. ORR data were collected at beginning of life (200 cycles) and after 12500 cycles and 25000 cycles. As expected, the presence of Nb increases the endurance of the Pt catalyst. PtNb/NbO_x-C, which has a 2-fold higher mass activity in comparison to Pt/C, retains the activity with a loss of 12.5% after 12500 cycles and 17.5% after 25000 cycles. However, Pt/C lost 15% activity after 12500 cycles and 34% activity after 25000 cycles. Such high tolerance toward catalyst degradation can be related to the presence of NbO_x moieties. In addition, under high operational voltage and oxidative environment, carbon is vulnerable to oxidation, especially in the presence of Pt that can destroy the integrity of the catalyst frame. Due to a stronger interaction between Pt and NbO_x, the mobility of the Pt atoms is lower on NbO_x in comparison to C, which in turn reduces the probability of catalyst degradation and particle agglomeration. It is also plausible that an electronic effect due to the existence of the Nb oxide dispenses extra stability to the platinum catalyst.

CO Stripping Experiments on PtNb/NbO_x-C Catalyst. The CO stripping reaction can lead to a deeper insight into the surface properties of an electrocatalyst, which is especially relevant in terms of investigating Pt−M bimetallic surfaces. This commonly studied reaction on Pt−M surfaces (M = binary metal) can be represented as

$$CO + Pt_{surf} \rightarrow Pt_{surf}CO$$

$$M_{surf} + H_2O \rightarrow M_{surf}OH_{ad} + H^+ + e^-$$

$$M_{surf}OH_{ad} + Pt_{surf}CO \rightarrow M_{surf} + Pt_{surf} + CO_2 + H^+ + e^-$$

In Figure 7, we have compared the CO stripping profiles of Pt/C and PtNb/NbO_x-C catalysts in acidic and alkaline environments. In acid electrolyte, the potential of zero charge of Pt/C is ∼0.63 V, beyond which the Pt surface begins to develop a positive charge, promoting adsorption of OH_{ad} species on the Pt surface as indicated in Figure 6a, inset. This phenomenon, in fact, matches with the onset of CO oxidation on Pt/C and is accompanied by a small prepeak at 0.72 V (Figure 7a). This prepeak at 0.72 V has been explained in terms of a sudden rise in coverage of OH_{ad} species formed via activation of water, which in turn expedites CO oxidation.[54] At 0.8 V, the OH_{ad} current reaches a peak as a consequence of an increase in coverage and stabilization of OH_{ad} on the Pt surface.[55] As expected, the CO oxidation peak on Pt/C is therefore located around 0.8 V as well. However, in PtNb/NbO_x-C catalyst, the adsorption of OH_{ad} species is significantly delayed as a consequence of shift of water activation to higher potentials (Figure 6a) and thus the onset of CO oxidation is shifted anodically to 0.72 V. Therefore, the CO stripping peak on PtNb/NbO_x-C is centered at 0.8 V and is devoid of any prepeak, unlike the case for Pt/C.

In alkaline electrolyte, the electrode−electrolyte interface is dramatically changed. Formation of OH_{ads} on pure Pt surface in alkaline media takes place as per the equation

$$Pt{-}OH_2{\cdots}OH{-}(HOH)_2 \leftrightarrow Pt{-}OH{\cdots}H{-}OH(HOH)_2 + e^- \quad \text{(i)}$$

The reversible potential associated with eq i is ∼0.17 V, indicating that it is thermodynamically possible for OH_{ad} to adsorb on Pt at such low potentials.[56] This phenomenon is facilitated by the presence of H_{ad} on Pt at the lower potentials, which imparts ∂^+ charge to Pt sites, allowing H_2O molecules to bond on the Pt surface by lone pair donation. The adsorbed water molecules then undergo reorientation and transfer of electrons and subsequently form Pt−OH_{ad} groups that are primarily responsible for the electro-oxidation of CO in alkaline electrolyte at lower potentials (∼0.3 V), as displayed in Figure 7a. Beyond 0.6 V, the Pt surface is strongly adsorbed by OH^- anions, which aid in oxidation of adsorbed CO, thereby explaining the sharp peak at 0.68 V.

DOI: 10.1021/acscatal.7b01061
ACS Catal. 2017, 7, 4936−4946

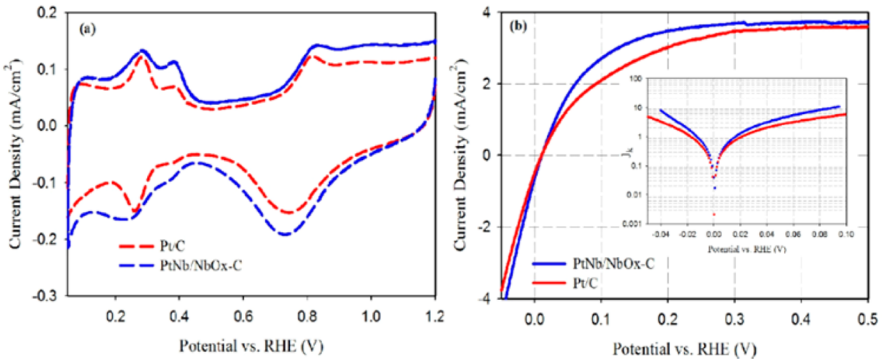

Figure 8. (a) Cyclic voltammogram of Pt/C and PtNb/NbO$_x$-C catalysts in deaerated 0.1 M KOH at 10 mV s^{-1} sweep rate. (b) HOR polarization curves collected for Pt/C and PtNb/NbO$_x$-C in H$_2$-saturated 0.1 M KOH at 1600 rpm and 10 mV s^{-1} scan rate. The inset gives the mass transport corrected kinetic current densities of Pt/C and PtNb/NbO$_x$-C.

From the above discussions, it can be inferred that, in alkaline media, strongly adsorbed H atoms on the Pt surface play a major role in facilitating electro-oxidation of CO at lower potentials. Interestingly, PtNb/NbO$_x$-C, does not exhibit a CO stripping onset until 0.4 V and features a single, sharper peak at 0.7 V which corresponds to the adsorption of OH$^-$ anions on the surface (Figure 7b). This indicates that, at the lower potentials, H$_{ads}$ may be weakly attached on the Pt surface in the case of PtNb/NbO$_x$-C catalyst, resulting in the anodic shift in the buildup of ∂^+ charge on Pt. As mentioned above at acidic pH, suppression of water activation provides for lower reactive OH$_{ad}$ species, thereby lowering site blocking in the context of ORR, providing a beneficial role. The CO stripping difference at this pH between Pt/C and PtNb/NbO$_x$-C is therefore consistent with this notion. At alkaline pH, however, the transition to potentials positive to zero charge brings serious competition with OH$^-$ species. The CO stripping behavior of PtNb/NbO$_x$-C catalyst in alkaline media brings up several questions regarding the H$_{ads}$–Pt interface in the low potential region that can be resolved using alkaline HOR experiments. Moreover, considering the unique structure of our catalyst, which has both metallic Nb alloyed with Pt and Nb oxides as support, it would be interesting to study the HOR considering the debates surrounding the mechanism of alkaline HOR (vide infra).

Alkaline Hydrogen Oxidation Reaction on PtNb/NbO$_x$-C Catalyst. Figure 8a compares the CVs of Pt/C and PtNb/NbO$_x$-C in 0.1 M KOH electrolyte. Per the hydrogen binding energy (HBE) theory, a difference in Pt–H binding energy is reflected in the position of the Pt–H$_{UPD}$ desorption (M–H$_{ad}$ → M + H$^+$ + e$^-$) peak. However, Pt/C and PtNb/NbO$_x$-C catalysts exhibit the H$_{UPD}$ desorption peak at the same potentials. While hydrogen binding energy theory emphasizes the effect of metal–adsorbate bond strength, reactive OH$_{ad}$ theory relates the kinetics of alkaline HOR to the availability of reactive OH$_{ad}$ species.[38] To test the validity and the contribution of these two theories in our system, we collected HOR polarization curves in alkaline media. Figure 8b shows the alkaline HOR activity of PtNb/NbO$_x$-C and Pt/C in 0.1 M KOH. The inset of Figure 8b shows the mass transport corrected kinetic current densities of Pt/C and PtNb/NbO$_x$-C. The exchange current densities extracted from this plot clearly validate that HOR kinetics on PtNb/NbO$_x$-C is significantly faster than on Pt/C. A quantitative comparison of the HOR performance of the two catalysts is illustrated in Table 2. At an overpotential of 50 mV, the specific activity of PtNb/NbOx-C is 4 mA/cm^2 in comparison to Pt/C, which executes a specific activity of only 0.5 mA/cm^2 (Figure S4 in the Supporting Information). Nb is a non-noble transition metal that is essentially passivated with an oxide or hydroxide layer in an alkaline electrochemical environment. As per reactive OH$_{ad}$ theory, such enhanced HOR activity of PtNb/NbO$_x$-C is due to the presence of surface oxides/hydroxides on Nb, which facilitate the extraction of hydrides from platinum surface to form water. It is known that the Nb surface is passivated and forms oxy-hydroxides at HOR potentials.[57] Following this hypothesis, it can be envisaged that the alloy formation between Pt and Nb is not mandatory for better HOR activity; rather, a close proximity of Pt and Nb may just be adequate to improve the HOR kinetics. To corroborate this, we further tested the HOR activity of some NbO$_x$-supported Pt catalysts where the interaction between Pt and Nb does not constitute a strong metal–metal alloy interaction in comparison to Pt–Nb alloys (PtNb/NbO$_x$-C) (Figure S5 in the Supporting Information). As shown in Figure S4 the niobia-supported Pt catalysts are much less active in comparison to PtNb/NbO$_x$-C. Hence, the reactive OH$_{ad}$ species theory does not seem to be decisive in appraising the HOR activity of Pt–Nb systems under alkaline conditions. The fact that there is an alloy formation in PtNb/NbO$_x$-C catalyst leads us to consider the electronic changes in Pt to be a strong contributor via engendering the weakening of the binding of hydrogen to the Pt surface. This, however, may not be discernible in the CV (Figure 8a). These results, in conjunction with the CO stripping results obtained in the previous section, strongly imply that the binding energy of hydrogen on Pt is altered in PtNb/NbO$_x$-C catalyst that, in turn, influences the mechanism of alkaline HOR. However, we also believe that neither reactive OH$_{ad}$ theory nor HBE theory is the sole descriptor of the activity of PtNb/NbO$_x$-C catalyst toward HOR$_{alkali}$; rather, it is a combination of both that determines the catalytic profile of PtNb/NbO$_x$-C.

Table 2. Quantitative Comparison of Pt/C and PtNb/NbO$_x$-C Catalysts in Terms of ECSA, Specific Activities (j_s), and Exchange Current Densities (i_0) toward Alkaline HOR[a]

catalyst	ECSA (m^2/g_{Pt})	j_0 (mA cm$^{-2}{}_{Pt}$)	j_s @ 50 mV (mAcm$^{-2}{}_{Pt}$)
Pt/C	65	0.56	0.5
PtNb/NbO$_x$-C	45	0.8	4

[a]The ECSA values were calculated from H$_{UPD}$ desorption area in 0.1 M HClO$_4$ electrolyte.

DOI: 10.1021/acscatal.7b01061
ACS Catal. 2017, 7, 4936–4946

CONCLUSION

In this report, we have assessed the catalytic profile of a platinum−niobium alloy supported on NbO_x and C which was synthesized in house. XRD and XAS experiments confirm the formation of an alloy between Pt and Nb. XPS data further affirm the presence of metallic Nb and Nb oxides on the surface of the catalyst as opposed to all oxides in the case of Pt supported on NbO_x. In situ XAS results illustrate the effect of Nb moieties on the electrochemical behavior of Pt. These results prove that Nb suppresses the adsorption of OH on Pt due to strong ligand effects and therefore enhances its catalytic activity toward the ORR. While the improved ORR activity and durability of PtNb/NbO_x-C catalyst is attributed to coalition of different interactions among Pt, Nb, NbO_x and C, the explanation of the superior HOR_{alkali} activity seems to be more intricate. By studying the CO stripping profiles of Pt/C and PtNb/NbO_x-C catalysts, we have tried to deduce the nature of Nb in PtNb/NbO_x-C catalyst in an operating electrochemical environment and have extended it to perceive the rationale behind the superior HOR_{alkali} performance. We believe the enhancement in HOR_{alkali} activity occurs because of interplay of both modified electronic structure (because of Pt−Nb interactions) and presence of reactive OH species (supplied by oxophilic Nb moieties). However, it is still unclear whether either of these two factors have dominance toward the observed HOR_{alkali} catalytic performance.

This work is an effort to encompass the wide spectrum of catalytic activity offered by Pt−Nb alloy in the presence of multiphase niobium moieties and to reach a consensus on the ongoing debate regarding HOR_{alkali} activity of Pt alloys. Further development on the current catalyst needs to be done to ensure higher ECSA and achieve better active site distribution for improved application in energy devices. To the authors' knowledge, this is the first reported work on Pt−Nb alloys, an interaction that has been mostly restricted to theoretical works. PtNb/NbO_x-C catalyst is a unique material that contains Nb in the form of oxides and metal. Such a singular frame aids in bringing the catalytic activity of Pt−Nb systems to the forefront for application in both acidic and alkaline energy conversion devices.

EXPERIMENTAL SECTION

Synthesis of PtNb/NbO_x-C Catalyst. The PtNb/NbO_x-C catalyst was prepared per Scheme 1, shown in this report. In a typical synthesis, 532 mg of $H_2Pt(OH)_6$ was dissolved in 30 mL of 6% SO_2 solution and stirred at room temperature for 24 h to form $H_3Pt(SO_3)_2(OH)$. After 24 h, a clear yellowish solution was obtained, which was transferred into a round-bottomed flask containing 50 mL of water and 750 mg of Vulcan carbon XC-72R, resulting in a black slurry. In a separate flask, 200 mg of $NbCl_5$ was dissolved in 1 mL of ethanol to obtain a clear solution. This solution was further treated with 8 mL of 0.3 M ammonia solution and 10 mL of 30% H_2O_2 solution to obtain peroxoniobic acid ($HNbO_4{\cdot}nH_2O$).[58] This resulting solution was then transferred to the black slurry via slow, dropwise addition at a controlled pH of 3.5. Once transferred, the slurry was heated at 85 °C for 30 min and eventually cooled to room temperature. It was then filtered, dried, and heated at 900 °C under a 5% H_2/Ar mixture for 8 h to give the final catalyst.

Physicochemical Characterization. X-ray diffraction characterization was done using a Rigaku Ultima IV XRD with Cu Kα source (λ = 1.541 Å) operated at 40 kV and 44 mA. $2\theta/\theta$ scans were conducted using a 0.05 step size and 5 s hold per step. Scanning electron microscopy (SEM) characterization was done using a Hitachi S-4800 FE-SEM. For validation of sample elemental composition, EDAX Genesis on the same SEM instrument was used. Transmission electron microscopy (TEM) and selected area electron diffraction (SAED) data were collected using a JEOL 2010 field emission gun at 200 kV accelerating voltage. The samples were deposited on a holey carbon film on a 300 mesh copper grid. X-ray photoelectron spectroscopy (XPS) data were acquired on a Kratos Axis Ultra DLD X-ray photoelectron spectrometer using a monochromated Al Kα source operating at 150 W. Acquisition times were 4 min for survey spectra, 14 min for Pt 4f spectra, and 16 min for Nb 3d spectra. Data analysis and quantification were performed using XPSpeak41 software. The depth of measurement was around 5−10 nm, and the spot size was 300 × 700 μm.

Electrochemical Characterization. All electrochemical measurements were done at room temperature using a rotating ring disk electrode (RDE) from Pine Instruments connected to an Autolab (Ecochemie Inc., Model PGSTAT 30) potentiostat/galvanostat. Tests were conducted in a 50 mL jacketed three-electrode cell in 0.1 M $HClO_4$ or 0.1 M KOH. For each test, a reversible hydrogen electrode (RHE), freshly made, was used as the reference electrode and a Pt-mesh wire was used as a counter electrode. A glassy-carbon disk (geometrical area of 0.245 cm^2) with a gold ring was used as the working electrode. All of the results shown here were collected after conditioning the electrodes at a scan rate of 50 mV/s for 30 scans between 0.05 and 1.0 V vs RHE, or until stable features were achieved.

In CO stripping experiments, CO was purged into the electrolyte for 10 min while the potential was held at 0.05 V vs RHE. Then argon was purged for 20 min to remove any dissolved CO in the electrolyte and to ensure that CO was present only at the electrode surface adsorbed on the catalyst. A linear scan was then started from 0.05 V at a scan rate of 10 mV/s.

Durability Measurements. To test the durability of the catalysts, a square-wave procedure was followed where the potential of the working electrode was stepped from 0.1 to 1.0 V (vs RHE) and held for 3 s. The potential of the working electrode was then stepped down to 0.1 V and held for another 3 s. Thus, each cycle would last for 6 s, and data were collected at the beginning of life (BOL) and after 12500 cycles and 25000 cycles.

X-ray Absorption Spectroscopy Measurements. In situ synchrotron XAS studies were conducted at the Pt (L_3 edge, 11564 eV) and Nb (K edge, 18986 eV) binding energies at the National Synchrotron Light Source (NSLS) at Brookhaven National Laboratories. A detailed description of the spectroelectrochemical cell is given in a previous publication from our group.[59] All of the data at the Pt L_3 edge and Nb K edge were collected in transmission mode. For transmission data, typically a three gas ionization detector (I_0, I_t/I_f, and I_{ref}) setup was used with 10% photon absorption in I_0 and 50−70% in I_t and I_{ref}. Typical loadings of the electrode used in these studies were based on the transmitted X-ray absorption cross section designed to provide a step height of unity. Nitrogen-saturated 0.1 M $HClO_4$ was used as the electrolyte along with an RHE prepared using the same electrolyte. Complete details of EXAFS analysis have been described in detail previously.[60] Briefly, IFEFFIT suite 1.2.9 was used for background subtraction using AUTOBK algorithm and normalization.

DOI: 10.1021/acscatal.7b01061
ACS Catal. 2017, 7, 4936−4946

The typical K-range window used was 3−14.0 $Å^{-1}$. The data were processed and fitted using the Athena[61] and Artemis[62] programs. The $\chi(R)$ transforms were modeled using single scattering paths calculated by the FEFF6 code.[63] In addition to the bulk averaged EXAFS analysis for obtaining short-range atomic order around Pt (bond distance, coordination number, Debye−Waller factor, etc.), surface-specific information was obtained using a previously developed subtractive method referred to as delta mu ($\Delta\mu$)[64] involving the near-edge part of the spectrum (X-ray absorption near-edge structure, XANES), where the effect of the invariant bulk signal was removed from the surface by subtracting XANES measured at a reference potential (0.1 V vs RHE) from other potentials of interest. Data analysis for $\Delta\mu$ studies at Pt L_3-edge X-ray absorption near-edge structure (XANES) spectra involved specific normalization procedures detailed elsewhere.[65] This involved careful calibration of edge energy (Pt L_3 edge, 11564 eV) and alignment to the standard reference scan to account for any drift in the beam energy. A post-edge normalization procedure was then applied to the aligned scans via a cubic spline function, which normalizes the oscillations over a specific energy range (typically 25−200 eV with respect to E_0), thus enabling normalized data on a per-atom basis. Difference spectra were obtained using the equation $\Delta\mu = \mu(V) - \mu(0.54\ V)$, where $\mu(V)$ is the XANES at various potentials and $\mu(0.54\ V)$ is the reference signal at 0.54 V, where the Pt surface is considered clean (i.e., free of surface adsorbates). These experimental difference signature profiles were then compared with theoretically generated profiles constructed using cluster models and the FEFF 8.0 code. Detailed modeling of the clusters in the context of surface-adsorbed species was not necessary in this study, as the primary focus was to examine the extent of susceptibility toward anion adsorption. Prior studies of such nature have been reported earlier.[66]

■ ASSOCIATED CONTENT

Supporting Information

The Supporting Information is available free of charge on the ACS Publications website at DOI: 10.1021/acscatal.7b01061.

Additional data on XPS, XAS, and electrochemical analyses (PDF)

■ AUTHOR INFORMATION

Corresponding Author

*S.M.: e-mail, s.mukerjee@neu.edu; tel, 617-373-2382; fax, 617-373-8949.

ORCID

Qingying Jia: 0000-0002-4005-8894

Jingkun Li: 0000-0003-1699-3089

Sanjeev Mukerjee: 0000-0002-2980-7655

Present Address

[#]Nano Terra, Inc., Cambridge, MA 02138, United States.

Notes

While this article is believed to contain correct information, Ford Motor Company (Ford) does not expressly or impliedly warrant, nor assume any responsibility, for the accuracy, completeness, or usefulness of any information, apparatus, product, or process disclosed, nor represent that its use would not infringe the rights of third parties. Reference to any commercial product or process does not constitute its endorsement. This article does not provide financial, safety, medical, consumer product, or public policy advice or recommendation. Readers should independently replicate all experiments, calculations, and results. The views and opinions expressed are of the authors and do not necessarily reflect those of Ford. This disclaimer may not be removed, altered, superseded or modified without prior Ford permission.

The authors declare no competing financial interest.

■ ACKNOWLEDGMENTS

Use of the synchrotron facilities at the National Synchrotron Light Source, beamlines X19A and X3B, at Brookhaven National Laboratory, Upton, NY, is supported by the U.S. Department of Energy, Office of Science, Office of Basic Energy Sciences, former under Contract No. DE-AC02-98CH10886. The authors thank Brookhaven National Laboratories for allowing us to work at National Synchrotron Light Source-I at beamlines X19A and X3B. This work was funded by the U.S. Department of Energy, Office of Basic Energy Sciences. The valuable assistance of Dr. Eric Farquhar and Dr. Syed Khalid is gratefully appreciated.

■ REFERENCES

(1) Mukerjee, S.; Srinivasan, S.; Soriaga, M.; McBreen, J. *J. Phys. Chem.* **1995**, *99*, 4577−4589.

(2) Paulus, U.; Wokaun, A.; Scherer, G.; Schmidt, T.; Stamenkovic, V.; Radmilovic, V.; Markovic, N.; Ross, P. *J. Phys. Chem. B* **2002**, *106*, 4181−4191.

(3) Mukerjee, S.; Srinivasan, S.; Soriaga, M. P.; McBreen, J. *J. Electrochem. Soc.* **1995**, *142*, 1409−1422.

(4) Strasser, P.; Koh, S.; Anniyev, T.; Greeley, J.; More, K.; Yu, C.; Liu, Z.; Kaya, S.; Nordlund, D.; Ogasawara, H. *Nat. Chem.* **2010**, *2*, 454−460.

(5) Scott, F. J.; Mukerjee, S.; Ramaker, D. E. *J. Phys. Chem. C* **2010**, *114*, 442−453.

(6) Kitchin, J. R.; Nørskov, J. K.; Barteau, M. A.; Chen, J. *Phys. Rev. Lett.* **2004**, *93*, 156801.

(7) Bligaard, T.; Nørskov, J. K. *Electrochim. Acta* **2007**, *52*, 5512−5516.

(8) Kitchin, J.; Nørskov, J. K.; Barteau, M.; Chen, J. *J. Chem. Phys.* **2004**, *120*, 10240−10246.

(9) Ruban, A.; Skriver, H. L.; Nørskov, J. K. *Phys. Rev. B: Condens. Matter Mater. Phys.* **1999**, *59*, 15990−16000.

(10) Wang, J. X.; Inada, H.; Wu, L.; Zhu, Y.; Choi, Y.; Liu, P.; Zhou, W.-P.; Adzic, R. R. *J. Am. Chem. Soc.* **2009**, *131*, 17298−17302.

(11) Zhang, J.; Lima, F.; Shao, M.; Sasaki, K.; Wang, J.; Hanson, J.; Adzic, R. *J. Phys. Chem. B* **2005**, *109*, 22701−22704.

(12) Toda, T.; Igarashi, H.; Uchida, H.; Watanabe, M. *J. Electrochem. Soc.* **1999**, *146*, 3750−3756.

(13) Mukerjee, S. *J. Appl. Electrochem.* **1990**, *20*, 537−548.

(14) Hou, Z.; Yi, B.; Yu, H.; Lin, Z.; Zhang, H. *J. Power Sources* **2003**, *123*, 116−125.

(15) Mukerjee, S.; Urian, R. C. *Electrochim. Acta* **2002**, *47*, 3219−3231.

(16) Neto, A. O.; Dias, R. R.; Tusi, M. M.; Linardi, M.; Spinacé, E. V. *J. Power Sources* **2007**, *166*, 87−91.

(17) Wang, J. X.; Ma, C.; Choi, Y.; Su, D.; Zhu, Y.; Liu, P.; Si, R. *J. Am. Chem. Soc.* **2011**, *133*, 13551−13557.

(18) Kepp, K. P. *Inorg. Chem.* **2016**, *55*, 9461−9470.

(19) Tanabe, K. *Catal. Today* **2003**, *78*, 65−77.

(20) Reichman, B.; Bard, A. J. *J. Electrochem. Soc.* **1980**, *127*, 241−242.

(21) Özer, N.; Rubin, M. D.; Lampert, C. M. *Sol. Energy Mater. Sol. Cells* **1996**, *40*, 285−296.

(22) Sasaki, K.; Zhang, L.; Adzic, R. *Phys. Chem. Chem. Phys.* **2008**, *10*, 159−167.

(23) Sasaki, K.; Adzic, R. *J. Electrochem. Soc.* **2008**, *155*, B180−B186.

DOI: 10.1021/acscatal.7b01061
ACS Catal. 2017, 7, 4936−4946

(24) Zhang, L.; Wang, L.; Holt, C. M.; Navessin, T.; Malek, K.; Eikerling, M. H.; Mitlin, D. *J. Phys. Chem. C* **2010**, *114*, 16463−16474.
(25) Ziolek, M. *Catal. Today* **2003**, *78*, 47−64.
(26) Ramaswamy, N.; Mukerjee, S. *Adv. Phys. Chem.* **2012**, *2012*, 1−17.
(27) Ramaswamy, N.; Tylus, U.; Jia, Q.; Mukerjee, S. *J. Am. Chem. Soc.* **2013**, *135*, 15443−15449.
(28) Yang, W.; Fellinger, T.-P.; Antonietti, M. *J. Am. Chem. Soc.* **2011**, *133*, 206−209.
(29) Blizanac, B. B.; Pylypenko, S.; Olson, T. S.; Konopka, D.; Atanassov, P. *J. Electrochem. Soc.* **2011**, *158*, B485−B491.
(30) Chun, H.-J.; Kim, D. B.; Lim, D.-H.; Lee, W.-D.; Lee, H. I. *Int. J. Hydrogen Energy* **2010**, *35*, 6399−6408.
(31) Greeley, J.; Stephens, I.; Bondarenko, A.; Johansson, T. P.; Hansen, H. A.; Jaramillo, T.; Rossmeisl, J.; Chorkendorff, I.; Nørskov, J. K. *Nat. Chem.* **2009**, *1*, 552−556.
(32) Sheng, W.; Gasteiger, H. A.; Shao-Horn, Y. *J. Electrochem. Soc.* **2010**, *157*, B1529−B1536.
(33) Sheng, W.; Myint, M.; Chen, J. G.; Yan, Y. *Energy Environ. Sci.* **2013**, *6*, 1509−1512.
(34) Conway, B.; Tilak, B. *Electrochim. Acta* **2002**, *47*, 3571−3594.
(35) Schmidt, T.; Ross, P.; Markovic, N. *J. Electroanal. Chem.* **2002**, *524-525*, 252−260.
(36) Durst, J.; Siebel, A.; Simon, C.; Hasche, F.; Herranz, J.; Gasteiger, H. *Energy Environ. Sci.* **2014**, *7*, 2255−2260.
(37) Sheng, W.; Zhuang, Z.; Gao, M.; Zheng, J.; Chen, J. G.; Yan, Y. *Nat. Commun.* **2015**, *6*, 5848−5853.
(38) Wang, Y.; Wang, G.; Li, G.; Huang, B.; Pan, J.; Liu, Q.; Han, J.; Xiao, L.; Lu, J.; Zhuang, L. *Energy Environ. Sci.* **2015**, *8*, 177−181.
(39) Strmcnik, D.; Uchimura, M.; Wang, C.; Subbaraman, R.; Danilovic, N.; van der Vliet, D.; Paulikas, A. P.; Stamenkovic, V. R.; Markovic, N. M. *Nat. Chem.* **2013**, *5*, 300−306.
(40) Schwämmlein, J. N.; El-Sayed, H. A.; Stühmeier, B. M.; Wagenbauer, K. F.; Dietz, H.; Gasteiger, H. A. *ECS Trans.* **2016**, *75*, 971−982.
(41) St. John, S.; Atkinson, R. W., III; Unocic, R. R.; Zawodzinski, T. A., Jr; Papandrew, A. B. *J. Phys. Chem. C* **2015**, *119*, 13481−13487.
(42) Thompson, S.; Jordan, L.; Shukla, A.; Forsyth, M. *J. Electroanal. Chem.* **2001**, *515*, 61−70.
(43) Stonehart, P. *Ber. Bunsenges. Phys. Chem.* **1990**, *94*, 913−921.
(44) King, H. *J. Mater. Sci.* **1966**, *1*, 79−90.
(45) Slater, J. C. *J. Chem. Phys.* **1964**, *41*, 3199−3204.
(46) Arruda, T. M.; Shyam, B.; Ziegelbauer, J. M.; Mukerjee, S.; Ramaker, D. E. *J. Phys. Chem. C* **2008**, *112*, 18087−18097.
(47) Greeley, J.; Mavrikakis, M. *Nat. Mater.* **2004**, *3*, 810−815.
(48) Kitchin, J.; Nørskov, J. K.; Barteau, M.; Chen, J. *J. Chem. Phys.* **2004**, *120*, 10240−10246.
(49) Bing, Y.; Liu, H.; Zhang, L.; Ghosh, D.; Zhang, J. *Chem. Soc. Rev.* **2010**, *39*, 2184−2202.
(50) Jia, Q.; Caldwell, K.; Strickland, K.; Ziegelbauer, J. M.; Liu, Z.; Yu, Z.; Ramaker, D. E.; Mukerjee, S. *ACS Catal.* **2015**, *5*, 176−186.
(51) Teliska, M.; Murthi, V. S.; Mukerjee, S.; Ramaker, D. E. *J. Electrochem. Soc.* **2005**, *152*, A2159−A2169.
(52) Zhang, L.; Wang, L.; Holt, C. M.; Zahiri, B.; Li, Z.; Malek, K.; Navessin, T.; Eikerling, M. H.; Mitlin, D. *Energy Environ. Sci.* **2012**, *5*, 6156−6172.
(53) He, Q.; Shyam, B.; Nishijima, M.; Ramaker, D.; Mukerjee, S. *J. Phys. Chem. C* **2013**, *117*, 4877−4887.
(54) Marković, N.; Schmidt, T.; Grgur, B.; Gasteiger, H.; Behm, R.; Ross, P. *J. Phys. Chem. B* **1999**, *103*, 8568−8577.
(55) Michaelides, A.; Hu, P. *J. Chem. Phys.* **2001**, *114*, 513−519.
(56) Anderson, A. B. *Electrochim. Acta* **2002**, *47*, 3759−3763.
(57) Robin, A. *Electrochim. Acta* **2004**, *49*, 1915−1923.
(58) Uekawa, N.; Kudo, T.; Mori, F.; Wu, Y. J.; Kakegawa, K. *J. Colloid Interface Sci.* **2003**, *264*, 378−384.
(59) Arruda, T. M.; Shyam, B.; Lawton, J. S.; Ramaswamy, N.; Budil, D. E.; Ramaker, D. E.; Mukerjee, S. *J. Phys. Chem. C* **2010**, *114*, 1028−1040.
(60) Jia, Q.; Liang, W.; Bates, M. K.; Mani, P.; Lee, W.; Mukerjee, S. *ACS Nano* **2015**, *9*, 387−400.
(61) Newville, M. *J. Synchrotron Radiat.* **2001**, *8*, 322−324.
(62) Ravel, B.; Gallagher, K. *Phys. Scr.* **2005**, *2005*, 606.
(63) Ankudinov, A.; Ravel, B.; Rehr, J.; Conradson, S. *Phys. Rev. B: Condens. Matter Mater. Phys.* **1998**, *58*, 7565.
(64) Jia, Q.; Caldwell, K.; Ziegelbauer, J. M.; Kongkanand, A.; Wagner, F. T.; Mukerjee, S.; Ramaker, D. E. *J. Electrochem. Soc.* **2014**, *161*, F1323−F1329.
(65) Arruda, T.; Shyam, B.; Ziegelbauer, J.; Ramaker, D.; Mukerjee, S. *ECS Trans* **2007**, *11*, 903−911.
(66) Ziegelbauer, J. M.; Gatewood, D.; Gullá, A. F.; Guinel, M. J.-F.; Ernst, F.; Ramaker, D. E.; Mukerjee, S. *J. Phys. Chem. C* **2009**, *113*, 6955−6968.

DOI: 10.1021/acscatal.7b01061
ACS Catal. 2017, 7, 4936−4946